

MERGING BINARY CLUSTERS

R. HANK DONNELLY¹, W. FORMAN¹, C. JONES¹, H. QUINTANA², A. RAMIREZ³, E. CHURAZOV^{4,5},
M. GILFANOV^{4,5}*accepted for publication in The Astrophysical Journal*

ABSTRACT

We study three prominent bi-modal X-ray clusters: A3528, A1750 and A3395. Using observations taken with *ROSAT* and *ASCA*, we analyze the temperature and surface brightness distributions. We also analyze the velocity distributions of the three clusters using new measurements supplemented with previously published data. We examine both the overall cluster properties, as well as the two sub-cluster elements in each. These results are then applied to the determination of the overall cluster masses, and demonstrate excellent consistency between the various methods used. While the characteristic parameters of the sub-clusters are typical of isolated objects, our temperature results for the regions between the two sub-clusters clearly confirm the presence of merger activity. These three clusters represent a progression of equal-sized sub-cluster mergers, starting from initial contact to immediately before first core passage.

Subject headings: galaxies: clusters: individual (A1750, A3395, A3528, SC0627-54) — galaxies: ICM — X-rays: galaxies

1. INTRODUCTION

Optical and X-ray studies (e.g. Forman et al. 1981; Geller & Beers 1982; Jones & Forman 1984; Dressler & Shectman 1988; Mohr et al. 1995; Bird 1994; Slezak et al. 1994) have shown that galaxy clusters are dynamically evolving systems, exhibiting a variety of substructure and asymmetric morphologies. The high frequency of substructure— $\sim 40\%$ (Forman & Jones 1990)—suggests that clusters are still forming hierarchically through the merger and accretion of subclusters and galaxy groups. While the prevalence of substructure has primarily been used to constrain cosmologies (Richstone, Loeb, & Turner 1992; Mohr et al. 1995), detailed studies of merging clusters impact a number of important areas including cooling flow formation and evolution, galaxy evolution, and gravitational mass measurements.

Temperature maps of the X-ray emitting gas are an especially sensitive tool for the detection of dynamic activity. Hydrodynamic simulations indicate that mergers should produce characteristic temperature patterns that survive 4-6 times longer than perturbations in the gas density (e.g. Schindler & Müller 1993; Ricker 1997). Recent observations (e.g. Henry & Briel 1995; Henriksen & Markevitch 1996; Markevitch et al. 1996a, 1998; Donnelly et al. 1998; Markevitch et al. 2000) have found just such characteristic temperature structures in a variety of clusters. In particular, in the earliest stages of a merger, simulations show the development of a shock located between the two sub-clusters and significant heating of the local ICM (Evrard 1990a and b; Schindler & Müller 1993).

Abell 3528, Abell 1750 and Abell 3395 are known as canonical binary galaxy clusters (Forman et al. 1981, Ray-

chaudury et al. 1991). All three exhibit two clearly separated peaks of emission in X-rays, and varying degrees of distortion in their X-ray surface brightness suggesting a progressive sequence of merging.

We used X-ray data from the *ROSAT* and *ASCA* satellites to characterize the emission profile of the gas as well as to map the distribution of temperatures and fit specific regions of interest with typical spectral models. We also analyzed optical velocity measurements to study the internal kinematics and overall dynamics of each cluster.

In Section 2 we discuss the data, its reduction and present the basic results of our work. Section 3 gives estimates of the masses determined from fitting the emission intensity profile, the X-ray luminosity and a virial estimate based on the velocities of the galaxies. Finally, we discuss the implications of our results in Sections 4 and 5 respectively. Throughout the paper we assumed $H_0 = 65 \text{ km s}^{-1} \text{ Mpc}^{-1}$, and the error bars quoted on all results are at the 1σ level.

2. OBSERVATIONS & METHODS

All three clusters—A3528, A1750, and A3395—were observed using both *ROSAT* and *ASCA*. Data were obtained from the HEASARC public archives and the details of the observations are given in Table 1. Using the broad energy response of *ASCA* (0.5-10.0 keV), these observations were used to accurately measure the gas temperatures and distributions in these clusters. The significantly better spatial resolution of *ROSAT* was used to determine the cluster surface brightness distribution, while *ROSAT* spectra of the central regions provided a diagnostic for the presence of cool gas.

We also compiled a list of velocities and positions of

¹Harvard-Smithsonian Center for Astrophysics, 60 Garden Street, Cambridge, MA 02138, USA²Department of Astronomy and Astrophysics, Pontificia Universidad Católica de Chile, Casilla 104, Santiago 22, CHILE³Department of Physics, Universidad de La Serena, Benavente 980, La Serena, CHILE⁴Max Planck Institute für Astrophysik, 85740 Garching bei München, GERMANY⁵Space Research Institute (IKI), Moscow 117810, RUSSIA

galaxies belonging to the three clusters using new data, supplemented with previously measured redshifts available from the literature. Using this data we analyzed the mean velocities and dispersions of the three clusters as well as sub-samples selected based on the X-ray emission. These results were then used to estimate the virial masses of the merging sub-clusters as well as a comparison to the X-ray results.

2.1. ASCA GIS

The *ASCA* GIS observations were “cleaned” using standard processing tools (Arnaud 1993) with a conservative version of the filtering criteria (ABC Guide⁶). The data from both GIS detectors was combined in our final analysis, while the SIS detectors, with their smaller field of view, were not used for this study.

To correctly characterize the temperature distribution of these extended sources, a correction for the energy dependent PSF must be applied (Takahashi et al. 1995). We employed a method developed by Churazov and Gilfanov (Churazov et al. 1996, hereafter the CG method), and used previously on other clusters (Donnelly et al. 1998, Donnelly et al. 1999, Churazov et al. 1999, and Henriksen et al. 2000). This method first explicitly corrects the core ($r \leq 6'$) PSF, then approximates the PSF of the wings via a Monte-Carlo simulation. The temperature is then fit in each 15" pixel using a linear combination of two fiducial single temperature spectra and smoothed at the resolution scale of the telescope ($\sim 5'$) to reduce noise. As shown for A1367 (Donnelly et al. 1998) the results of this method are fully consistent with those found using the method presented by Markevitch et al. (1996 and 1998).

Applying this method to each of our three clusters, we fit a Raymond-Smith model to the emission from the entire cluster to derive a global gas temperature (T_{ASCA}). The results are given in Table 2. However, the CG method also allowed us to generate two dimensional continuous maps of the gas temperature distributions within the clusters. These temperature maps are shown in Figures 1-3 (top left).

Finally, we also used the CG method to define discrete regions on each cluster and fit the temperature within each region, as shown in Figures 1-3. In each cluster we defined a region around the core of each sub-cluster, two regions to the “outside” – i.e. away from the other sub-component, and a region between the two subclusters. The fit temperatures, with the associated uncertainties, for these regions are shown in the bottom left of Figures 1-3.

2.2. ROSAT PSPC

The *ROSAT* PSPC data were reduced using the standard procedures outlined by Snowden (1994; see also Snowden et al. 1994). By combining only the data from bands 4 through 7 (0.44-2.04 keV), we excluded the lowest energies, that generally have higher X-ray background.

For each of the six sub-clusters in the sample, we generated radial surface brightness profiles in 1' annuli centered on the peak emission for each sub-component. The annuli extended from 0' to 45' and, to minimize contamination of the intensity profile, we excluded the azimuthal half of the profile toward each sub-component's

partner. We then measured the average surface brightness ($\text{cts s}^{-1} \text{arcmin}^{-2}$) in each annulus and fit the resultant surface brightness profile with a standard hydrostatic, isothermal β -model:

$$\Sigma(r) = \Sigma_0 \left[1 + \left(\frac{r}{r_c} \right)^2 \right]^{-(3\beta - \frac{1}{2})} \quad (1)$$

(Cavaliere & Fusco-Femiano 1976). The backgrounds were fit by including a constant component in our models. For A1750 and A3395 the backgrounds fell in the range $2.08 - 2.80 \times 10^{-4} \text{ cts s}^{-1} \text{arcmin}^{-2}$, consistent with typical PSPC backgrounds. For both clusters the errors for the two sub-clusters were consistent with single constant backgrounds. A3528 lies near the edge of its *ROSAT* frame (an AGN is actually the target of this observation). We used a nearby region of sky to determine the background and found a count rate of $2.43 \times 10^{-4} \text{ cts s}^{-1} \text{arcmin}^{-2}$ that was included in our fits for this cluster. The bolometric luminosity for each sub-cluster was also calculated using the same regions. The global fit results and luminosities are given in Table 2.

To search for evidence of the presence of cool gas within the cores, we also extracted *ROSAT* spectra from the central 2' of each sub-cluster. Using XSPEC to fit a single temperature Raymond-Smith model to the data, we confirmed the presence of cool gas in the NE sub-cluster of A1750 ($T = 1.9^{+1.3}_{-0.5}$ keV) and both subclusters in A3528 ($T_{SE} = 2.1^{+0.7}_{-0.4}$ keV and $T_{NW} = 2.3^{+1.3}_{-0.5}$ keV).

2.3. OPTICAL SPECTROSCOPY

A3395 was observed with the ARGUS fiber spectrograph at the CTIO 4m telescope, and with the Shectograph detector at the 100" DuPont telescope at the Las Campanas Observatory (LCO). The Shectograph/100" combination at LCO also was used for all of the spectroscopic observations of A1750. Specifics of the instrumental set ups, observing details, reduction and calibration procedures, as well as an evaluation and discussion of internal and external errors, are given in Quintana & Ramírez (1990). For A3528 the data were drawn from the work by Quintana et al. (2000) on the Shapley Supercluster. The interested reader is directed to that work for a complete discussion of the instrumental configuration.

Velocity determinations were carried out using both a cross-correlation technique and by identifying and fitting line profiles. All reductions were performed using the LONGSLIT, ONEDSPEC and RVSAC packages in IRAF. No systematic internal errors or zero point corrections were found. Typical uncertainties for individual spectra were 30-40 km s⁻¹ using the line fitting method. Cross-correlation was applied following the procedures described in Quintana, Ramírez, & Way 1995 (QRW95) using 8 templates. In this case the errors were somewhat higher (40-50 km s⁻¹) compared to the line fitting method. There was no velocity offset between the methods, and the cross-correlation was not applied to spectra with emission lines.

We expect some systematic shifts between velocities for A3395 derived from the two different instrument/telescope configurations (LCO 2.5m and CTIO 4m). We confirmed

⁶See <http://heasarc.gsfc.nasa.gov/docs/asca/abc/abc.html>

this on a wider data sample, as discussed in QRW95. Following the discussion there, for the present set, we combined velocities after correcting for a 50 km s⁻¹ shift between ARGUS and Shectograph data.

For all three clusters we excluded a small number of objects with obviously discrepant velocities (i.e. a velocity more than 5,000 km s⁻¹ greater or lesser than the peak of the cluster distribution). In the case of A3528 this included 18 objects centered around 23,000 km s⁻¹. These objects are scattered around the field and may represent a background group.

The data for all three clusters also were supplemented by redshifts available through the NASA/IPAC Extragalactic Database (NED). For A3528 four velocities were drawn from Katgert et al. (1998), although, no attempt at a determination of a systematic offset was attempted due to the small sample size. The full listing is given in Table 3.

The NED data for A1750 are from Beers et al. (1991) which shares 26 galaxies with our new data (67 galaxies). From a comparison of the velocities of these common objects, we find that our velocities are systematically larger by 69 km s⁻¹. In order to have all of our data in a self-consistent frame, we have applied this offset to the NED data and the offset values are listed in Table 4.

Similarly for A3395, we have 54 Shectograph velocities in common with Teague, Carter & Gray (1990, TCG90) with a systematic offset of 82 kms⁻¹. In the case of the ARGUS data, there are 24 velocities in common with TCG90 and our velocities are larger by 133 kms⁻¹. Both offsets were applied to the NED data and final velocities are listed in Table 5. There are two galaxies observed with ARGUS and published in TCG90 with large discrepant velocities, both with a TCG90 R value below ~ 2.5 , that we included in the cluster redshift, contrary to TCG90 who believe them to be background galaxies.

When galaxies had more than one velocity, we adopted as the final value the weighted mean velocity and the associated uncertainty. Weighting factors came from the published uncertainties combined with our internal uncertainties. More details about this procedure are extensively discussed in QRW95.

Using the statistical prescriptions described in Beers et al. (1990) we determined the “mean” velocity for each of our three clusters (see Tables 2 and 6). We find generally excellent agreement with previous results (Abell, Corwin, & Olowin 1989, Struble & Rood 1999). One exception is that for A3528. Our results give a “mean” velocity more than 500 km s⁻¹ larger than that found by Struble & Rood (1999), but which is more consistent with the values found previously for this cluster by Abell, Corwin, & Olowin (1989) and Katgert et al. (1996).

The positions of the galaxies are shown with the X-ray intensity isophotes from *ROSAT* overlaid in Figures 1-3. We expanded the field of view from that shown for the temperature maps to include all of the galaxies that appear to be members of each cluster. Galaxies with lower velocities than our “mean” cluster velocity are shown in blue while those with higher velocities are shown in red. A velocity histogram for each cluster is also presented.

We note that A3395 has a high velocity bump in its distribution. These objects are shown in Figure 3 as open circles. While they are localized in velocity space, they are distributed very widely across the field of view. This sug-

gests that it is unlikely that they are a background group, and thus they have simply been included in the overall sample.

3. RESULTS AND ANALYSIS

3.1. MASSES

We first estimated the mass of the X-ray emitting gas by using the luminosities for the sub-clusters determined from the *ROSAT* data and solving for the central density (given in Table 2),

$$L(r) = \frac{2\pi n_e n_H \Lambda_0 r_c^3}{(1 - 3\beta)} \times \int_0^\infty \left[\left(1 + s^2 + \left[\frac{r}{r_c} \right]^2 \right)^{-3\beta+1} - (1 + s)^{-3\beta+1} \right] ds \quad (2)$$

(David et al. (1990). The gas density distribution is then integrated to the radius of interest,

$$M_{gas}(r) = 4\pi \rho_0 \int_0^r s^2 \left[1 + \left(\frac{s}{r_c} \right)^2 \right]^{-\frac{3\beta}{2}} ds \quad (3)$$

Gas masses within 0.5 and 1.0 Mpc are given in Table 7.

We estimated the total mass of each sub-cluster assuming spherical symmetry, hydrostatic equilibrium and using our fit values for the core radii and β ’s. With these assumptions the mass contained within a radius r is,

$$M(< r) = -\frac{kT(r)}{\mu m_p G} \left(\frac{d \log \rho_g(r)}{d \log r} + \frac{d \log T(r)}{d \log r} \right) r. \quad (4)$$

Markevitch et al. (1998, 1999) found that the temperature profiles of galaxy clusters are well approximated by a polytropic equation of the form,

$$T \propto (1 + r^2)^{-\frac{3}{2}\beta(\gamma-1)} \quad (5)$$

where $\gamma \simeq 1.24$. Using this function for the temperature, Equation 4 reduces to

$$M(r) = 3.70 \times 10^{13} M_\odot \frac{0.60}{\mu} T(r) r \frac{3\beta\gamma r^2}{r_c^2 + r^2}, \quad (6)$$

where $T(r)$ — derived from the fit temperature in the core of each sub-cluster— and r are measured in keV and Mpc respectively. However, recent work (Arnaud et al. 2001) done with data taken from *XMM* suggests that clusters are actually isothermal. If this is the case then our estimates of the total mass are too high by a factor of 1.24. Table 7 gives the results for both the non-isothermal and isothermal total masses. We have also included the total (non-isothermal) mass within 0.5 Mpc for comparison with the gas mass at the same radius.

Evrard et al. (1996) suggested that cluster scaling relations also provide reliable estimates of the mass. A volume with an overdensity of δ_c has a total mass of

$$M(r < r_{\delta_c}) = \delta_c \frac{4}{3} \pi \rho_{crit} r_{\delta_c}^3. \quad (7)$$

Inverting the scaling relation between radius and temperature (Mohr et al. 2000),

$$r_{\delta_c} = \frac{(aT)^{\frac{1}{2}}}{(\delta_c \rho_{crit})^{\frac{1}{2}}} \quad (8)$$

to solve for δ_c , we find that

$$M(r < r_{\delta_c}) = \frac{4}{3} \pi a T r_{\delta_c} \quad (9)$$

For comparison we calculate the mass contained within 1 Mpc. Taking the result from Mohr et al. (2000) that $r_{200} = 4h_{50}^{-1}$ Mpc for a 10 keV cluster in our cosmology, Equation 9 then reduces to

$$M(r < 1 \text{ Mpc}) = 9.30 \times 10^{14} \left(\frac{T}{10 \text{ keV}} \right) M_{\odot}. \quad (10)$$

The masses within 1 Mpc for each subcluster using the fit temperature from the core can be found in Table 7. Our results using the scaling relation are generally consistent with those derived from the luminosity and intensity profiles.

The cluster velocity distributions also demonstrate typical dispersions with scales of order 1000 km s⁻¹. Again employing the statistical methods of Beers et al. (1990), we examined the characteristics of velocity distributions of each core. In order to isolate each sub-cluster in our analysis we selected only galaxies that lay within a projected radius of 0.5 Mpc of each sub-cluster center. Table 6 gives the details of the velocity distributions and is consistent with typical sub-cluster sized systems.

Two circles indicate the radial extent of the two different subcluster core elements the surface distribution maps of the galaxies in Figures 1, 2 and 3. The velocity histograms of the two core samples in each cluster have been color coded to the circles and shown along with the overall velocity histograms. For A3395 the two cores are in such close proximity that the 0.5 Mpc circles overlap and there are nine objects in common. The measured dispersions reported in Table 6 for the two sub-samples in A3395 were performed both including and excluding the disputed objects. These objects were excluded from the sub-clump velocity histograms with the number of disputed galaxies in each bin indicated above that bin.

Following the approach outlined by Beers, Geller and Huchra (1982), we estimated the entire total mass of each sub-cluster using virial techniques. Assuming that they are bound and the velocity dispersions are isotropic, the total mass of each sub-cluster is

$$M_{virial} = \frac{3\pi}{G} \sigma_r^2 \left\langle \frac{1}{r_p} \right\rangle^{-1}, \quad (11)$$

where σ_r is the velocity dispersion along the line of sight and $\left\langle \frac{1}{r_p} \right\rangle^{-1}$ is the harmonic mean projected separation on the sky. The masses and values for $\left\langle \frac{1}{r_p} \right\rangle^{-1}$ are given in Tables 7 and 2 respectively. We note that while the radial restriction of the galaxy sample should not affect the determination of the velocity dispersion, it may lead to a small underestimate of the mean harmonic radius and thus

also the calculated virial masses. Except for the southeast element of A3528, all of the results are in good agreement with the determination from the X-ray data of the integrated total mass within 1 Mpc.

For the southeast clump of A3528, whose optically determined virial mass is twice the X-ray derived total mass, we note that the velocity distribution for this sub-clump has a very extended tail with two galaxies having rather large relative velocities ($\delta V = 1069$ and 1554 km s^{-1}) compared to the mean sub-clump velocity. If these two galaxies are excluded from the velocity calculations for the southeastern clump, the dispersion drops from 930 km s^{-1} to 513 km s^{-1} . While the average projected distance increases slightly with this exclusion, the overall effect is to reduce the estimated virial mass by nearly a factor of three, which brings it into much better agreement with the total mass within 1 Mpc.

4. DISCUSSION

Our data suggest that these three clusters represent progressive stages of first time merger events prior to first core passage. A3528, with its very azimuthally symmetric intensity isophotes appears to be at the earliest stage, when gas in the outer halos of the sub-clumps is just beginning to interact. In A1750, the effects of the merger have begun to distort the intensity isophotes, while A3395 with its clearly disrupted intensity distribution appears to be nearly at first core passage.

Other than their merger state, all three clusters appear to be generally normal. They all have gas mass fractions of $\sim 20\%$ at 0.5 and $\sim 30\%$ at 1.0 Mpc, and their fit β values and core radii (Table 2) are typical for galaxy clusters (Jones & Forman 1984, Jones & Forman 1999, and Vikhlinin et al. 1999).

The temperature maps of all three clusters have elevated gas temperatures in the region between the two emission peaks. For all three, the deviation from the overall mean temperature is significant at the 90% confidence level. We note that the heated gas does not have a significant impact on the global fit temperature for each cluster because of its significantly smaller contributions to the overall intensities.

In A3528 the deviation between the merger region (region 3 for all three clusters) and the other regions is the least pronounced and could still be consistent with a uniform temperature throughout the entire cluster— excepting the far northeastern side where the temperature is especially low.

We find a similar result for the temperature data from A1750, although the temperature of the merger region is inconsistent with the temperature of the southwestern core. This suggests that a shock region is developing in the gas, as it is compressed between the two sub-clusters.

Finally, A3395 clearly demonstrates the compression and concomitant heating of the gas that would be expected in merger events similar to those modeled by Roettiger, Burns & Loken (1996; see also Roettiger, Loken & Burns 1997) and Norman & Bryan (1999).

The spectral analysis of the *ROSAT* data in the sub-cluster cores indicates that cool gas is still present in both core elements in A3528 and the northeastern clump of A1750 but not in the other cores. This is consistent with

a scenario where the gas within the core is heated as the merger process proceeds.

Since only A3395 shows significantly higher gas temperatures between the sub-clusters, which we interpret as being due to the merger of these sub-clusters, we tested whether or not the systems were bound by examining the overall dynamics of these clusters. A bound system must necessarily fulfill the simple Newtonian energy consideration:

$$V_r^2 R_p \leq 2GM \sin^2 \alpha \cos \alpha, \quad (12)$$

where V_r is the observed relative radial velocity, R_p is the projected separation of the two sub-clusters, M is the sum of the masses of the two sub-clumps (i.e. the entire system) and α is the projection angle from the plane of the sky. Plots for all three clusters are presented in Figure 4.

The dashed line separates the bound configurations (to the left) from the unbound configurations. We included our measurement of the relative velocity as a solid vertical line with a one sigma confidence region marked by cross-hashings. From Figure 4 it is clear that every reasonable configuration for both A3528 and A3395 indicates that the systems are bound.

For A1750 the dynamical analysis is less conclusive. This is in contrast to similar previous work on this cluster by Beers et al. (1991). While our mass for this cluster is only slightly smaller than their “doubled” mass simulation (6.1 vs $6.8 \times 10^{14} M_\odot$), the larger R_p , implied by our cosmology, and the increase in V_r , from our improved velocity sample decrease the likelihood that the system is bound. However, we note that A1750 has two other components to the system (Beers et al. 1991, Einasto et al. 1997, Jones & Forman 1999) whose mass had not been included in our simple model. The inclusion of these masses would certainly strongly increase the likelihood that a purely dynamical analysis would find the system to be bound.

5. SUMMARY

Using observations from *ROSAT* and *ASCA*, we developed temperature and density distributions for the hot X-ray emitting gas in three binary galaxy clusters: A3528, 1750 and 3395.

We find that the values for β , R_c and the luminosities, as well as the masses derived from these parameters, are typical of single clusters. For A3528 and A1750 this is not particularly surprising, given that the bulk of the photons which determine the fit are derived from the core regions which in general are much less distorted than the outer isophotes. However, it is interesting that A3395 which is clearly strongly distorted, still maintains an intensity profile typical of relaxed unperturbed clusters.

Using new velocity data, supplemented with measurements from the literature for each cluster, we generated estimates of the mean velocities for the sub-clusters as well as for the overall cluster, estimates of the dispersions (the “scale” of the distributions) and velocity histograms. Two of the clusters (A3528 and A3395) show no significant differences in the velocities of the subclusters and thus the in-fall appears to be nearly in the plane of the sky. For A1750 the velocity difference of the subclusters is 1335 km s^{-1} , suggesting that the merger lies more along the line of sight. The masses estimated using the virial method are consistent with the X-ray derived masses.

We also produced an analysis of their orbital dynamics from simple Newtonian energy considerations and find that A3528 and A3395 are nearly certainly bound to each other. The results for A1750 are less conclusive, however as we note there are several nearby additional mass components that are not included in our estimates of the total mass but which are likely part of the same structure and would strongly increase the probability that the system is bound.

The temperature results indicate some heating of the intra-cluster gas, consistent with the level of disruption of the surface brightness distributions. The most prominent feature is the heating of the gas located between the sub-clusters of each binary. In addition, the absence of cool gas in the cores of three of the subclusters (both parts of A3395 and the southwest element of A1750) may have resulted from the disruption of the cooling flow by the merger.

Our observations suggest that A3528 is in the early stages of a merger, where the gas in both sub-clusters is only just beginning to interact. Both cores show evidence of cool gas, and the intensity contours are still azimuthally symmetric. The temperature of the gas located between the sub-clusters is marginally hotter ($\sim 15\%$) than the overall average for the cluster.

A1750 is slightly further along in the merging process. One of the sub-clusters retains cool gas in the core, but the other most likely does not. There is some elongation of the intensity isophotes and the gas between the cores shows significant heating to $\sim 30\%$ above the overall average.

Finally, A3395 is nearly at first core passage. Neither core shows evidence for cool gas, the intensity isophotes are highly disrupted and the temperature distribution clearly shows that the gas between the two sub-clusters has been heated $\sim 30\%$ above the overall average.

Taken together these three binary clusters present a sequence of views of a typical merger event in a galaxy cluster. More detailed spectroscopic studies with *CHANDRA* and *XMM* will provide details of the merging process and its effects on both the intra-cluster medium and the resident galaxies.

TABLE 1
OBSERVATIONAL DATA

Cluster	ROSAT			ASCA				
	α (J2000)	δ (J2000)	Sequence #	Date	Live Time (ksec)	Sequence #	Date	On Time (ksec)
A3528	12:54:29	-29:07:00	300093	7/16/96	15.0	84057000	1/15/96	18.9
A1750	13:31:00	-1:47:18	800553	7/01/93	12.7	81010000	1/27/94	33.5
A3395	6:27:03	-54:08:48	800079	7/16/91	2.6	82033000	2/14/95	31.1

TABLE 2
CLUSTER PROPERTIES

Cluster	z	L^a (10^{45} ergs s $^{-1}$)	T_{ASCA} (keV)	β	r_c (Mpc)	$n_e(0)$ (10^{-3} cm $^{-3}$)	$\langle \frac{1}{r} \rangle^{-1}$ (Mpc)
A3528 SE	0.0545	2.85	4.7 ± 0.3	$0.55^{+0.02}_{-0.01}$	$0.14^{+0.02}_{-0.02}$	12.48	$0.35(0.39)^b$
A3528 NW		2.02		$0.59^{+0.04}_{-0.04}$	$0.14^{+0.03}_{-0.02}$	11.45	0.22
A1750 NE	0.0855	1.72	3.6 ± 0.2	$0.52^{+0.04}_{-0.03}$	$0.17^{+0.04}_{-0.02}$	6.99	0.20
A1750 SW		2.37		$0.65^{+0.04}_{-0.04}$	$0.23^{+0.04}_{-0.02}$	8.10	0.22
A3395 NE	0.0506	2.07	4.5 ± 0.2	$0.66^{+0.26}_{-0.13}$	$0.32^{+0.18}_{-0.11}$	4.74	0.23
A3395 SW		2.22		$0.60^{+0.23}_{-0.12}$	$0.28^{+0.18}_{-0.11}$	4.86	0.28

^aLuminosities are bolometric values from *ROSAT* data within 1 Mpc of each sub-cluster core.

^bThe parenthetical value excludes the two galaxies with highly discrepant velocities.

TABLE 3
ABELL 3528 VELOCITIES

α (J2000)	δ (J2000)	v (km s $^{-1}$)	Reference	α (J2000)	δ (J2000)	v (km s $^{-1}$)	Reference
12:52:37.8	-28:54:47	16052 \pm 50	1	12:54:35.7	-29:06:38	16254 \pm 60	1
12:53:15.9	-29:19:04	16403 \pm 50	1	12:54:38.4	-28:58:56	17101 \pm 50	1
12:53:26.1	-28:54:11	16336 \pm 61	1	12:54:39.8	-28:56:32	15759 \pm 51	1
12:53:31.2	-29:27:18	15201 \pm 61	1	12:54:39.8	-29:27:33	15045 \pm 59	1
12:53:40.6	-28:48:58	16633 \pm 132	1	12:54:40.5	-29:01:49	15827 \pm 50	2,3
12:53:45.6	-29:02:53	14872 \pm 48	2	12:54:41.0	-28:53:00	16432 \pm 50	1
12:53:52.0	-28:36:15	14791 \pm 50	1	12:54:41.0	-29:13:37	16783 \pm 123	1
12:53:54.6	-28:34:04	14671 \pm 50	1	12:54:42.5	-29:01:00	22737 \pm 50	1
12:53:58.2	-29:31:09	17631 \pm 52	1	12:54:43.1	-28:52:16	16237 \pm 50	1
12:54:00.8	-28:44:07	16680 \pm 50	1	12:54:48.6	-29:12:00	15824 \pm 79	1
12:54:01.6	-28:30:00	16528 \pm 50	1	12:54:49.2	-29:09:54	17260 \pm 70	1
12:54:03.9	-29:04:22	17303 \pm 50	1	12:54:50.7	-28:41:47	14560 \pm 50	1
12:54:10.6	-29:10:41	17177 \pm 50	1	12:54:52.2	-29:16:16	14486 \pm 50	1
12:54:11.3	-29:01:46	16622 \pm 50	1	12:54:52.4	-28:43:17	16986 \pm 73	1
12:54:12.1	-29:09:22	15894 \pm 50	1	12:54:53.2	-28:31:58	15426 \pm 50	1
12:54:14.3	-28:59:16	16784 \pm 50	1	12:54:53.9	-29:00:46	16174 \pm 70	1
12:54:15.6	-29:00:19	15437 \pm 86	1	12:54:55.3	-29:30:11	16329 \pm 137	1
12:54:16.3	-28:45:23	15548 \pm 50	1	12:54:56.2	-28:55:40	15926 \pm 50	1
12:54:16.9	-29:01:16	15119 \pm 50	1	12:54:56.4	-29:06:28	13816 \pm 100	1
12:54:17.6	-29:00:47	16186 \pm 113	1	12:55:04.3	-29:15:56	17007 \pm 57	2
12:54:18.9	-29:18:11	16083 \pm 54	2	12:55:18.6	-29:12:04	16866 \pm 68	1
12:54:20.5	-29:04:10	16287 \pm 50	1	12:55:19.7	-29:17:20	16476 \pm 54	2
12:54:21.5	-29:13:23	16834 \pm 50	1	12:55:21.0	-28:57:01	15834 \pm 65	1
12:54:22.2	-29:00:45	16219 \pm 50	1	12:55:27.6	-28:47:50	17487 \pm 51	1
12:54:22.9	-29:04:17	17391 \pm 71	1	12:55:29.6	-28:45:35	17367 \pm 109	1
12:54:23.3	-29:01:05	16353 \pm 63	3	12:55:33.0	-28:48:52	17740 \pm 69	1
12:54:23.5	-29:10:02	16530 \pm 50	1	12:55:40.2	-28:34:33	17073 \pm 50	1
12:54:24.7	-28:59:36	16914 \pm 50	1	12:55:43.6	-29:24:41	18479 \pm 94	1
12:54:25.3	-28:58:24	14664 \pm 50	1	12:55:44.8	-29:01:11	16810 \pm 50	1
12:54:26.7	-28:57:20	15720 \pm 50	1	12:55:50.8	-28:45:16	16298 \pm 50	1
12:54:28.1	-28:57:42	14122 \pm 50	1	12:55:57.5	-29:17:58	16757 \pm 57	1
12:54:28.1	-29:00:42	13413 \pm 260	1	12:56:13.0	-29:13:44	16825 \pm 118	1
12:54:28.8	-29:17:31	14971 \pm 63	1	12:56:20.9	-28:59:14	17885 \pm 54	1
12:54:31.5	-28:55:18	16790 \pm 50	1	12:56:24.9	-29:12:59	16963 \pm 50	1
12:54:35.3	-29:04:41	16217 \pm 55	1	12:56:27.6	-29:08:54	17825 \pm 79	1
12:54:35.4	-29:00:39	14713 \pm 50	1	12:56:27.9	-29:08:55	17719 \pm 50	1

REFERENCES.— (1)Quintana et al. 2000; (2)Katgert et al. 1998 ; (3)Quintana et al. 1995

TABLE 4
ABELL 1750 VELOCITIES

α (J2000)	δ (J2000)	v (km s $^{-1}$)	Reference	α (J2000)	δ (J2000)	v (km s $^{-1}$)	Reference
13:30:15.2	-1:31:09	27131 \pm 28	1	13:30:57.4	-1:44:31	22939 \pm 20	1,2
13:30:18.4	-2:00:48	26145 \pm 23	1,2	13:30:58.2	-1:51:13	25413 \pm 50	1
13:30:18.7	-1:32:44	24826 \pm 22	1	13:30:59.8	-1:43:36	24780 \pm 40	1,2
13:30:32.3	-1:47:36	26297 \pm 28	1	13:31:01.2	-1:50:52	26012 \pm 30	1,2
13:30:32.9	-1:39:35	25171 \pm 35	1	13:31:04.7	-1:38:04	24665 \pm 33	1
13:30:34.4	-1:47:45	25034 \pm 34	1	13:31:06.1	-1:40:48	25184 \pm 30	1,2
13:30:34.5	-1:48:27	26354 \pm 100	2	13:31:06.4	-1:44:14	24400 \pm 50	2
13:30:35.1	-1:49:05	24543 \pm 36	1	13:31:09.7	-1:44:45	25229 \pm 50	2
13:30:36.8	-1:53:04	25951 \pm 23	1,2	13:31:09.9	-1:41:09	24510 \pm 20	1,2
13:30:38.2	-1:50:36	25598 \pm 24	1,2	13:31:10.4	-1:38:03	25880 \pm 37	1
13:30:48.9	-1:53:56	27585 \pm 46	1,2	13:31:10.8	-1:43:49	25019 \pm 41	1,2
13:30:41.4	-1:41:14	26165 \pm 44	1	13:31:11.0	-1:43:41	25058 \pm 26	1,2
13:30:42.5	-1:51:24	25247 \pm 26	1,2	13:31:11.2	-1:43:35	25381 \pm 24	1,2
13:30:44.4	-1:53:19	26408 \pm 23	1,2	13:31:13.3	-1:58:42	26903 \pm 38	1
13:30:44.5	-1:59:29	24809 \pm 30	1	13:31:13.9	-1:48:58	25740 \pm 38	1
13:30:45.5	-1:48:43	24051 \pm 57	2	13:31:14.7	-1:30:17	25461 \pm 37	1
13:30:46.1	-1:52:28	26434 \pm 31	1,2	13:31:16.2	-1:59:35	27684 \pm 43	1
13:30:48.1	-1:52:02	26231 \pm 32	1,2	13:31:19.3	-1:42:19	24339 \pm 50	2
13:30:48.1	-1:52:12	25118 \pm 25	1,2	13:31:19.5	-1:45:39	24522 \pm 27	1,2
13:30:48.5	-1:37:48	25100 \pm 42	1	13:31:22.2	-1:43:14	24933 \pm 50	2
13:30:49.0	-1:52:52	27926 \pm 50	2	13:31:23.1	-2:01:37	26731 \pm 45	1
13:30:49.1	-1:53:56	27361 \pm 50	2	13:31:23.4	-1:43:35	22724 \pm 23	1,2
13:30:49.8	-1:40:40	24328 \pm 20	1	13:31:23.9	-1:53:35	26343 \pm 37	1
13:30:50.1	-1:47:55	26260 \pm 30	1,2	13:31:27.9	-1:43:50	25260 \pm 41	2
13:30:50.4	-1:51:27	26086 \pm 24	1,2	13:31:30.0	-1:39:25	25259 \pm 24	1,2
13:30:50.5	-1:51:44	26472 \pm 29	1,2	13:31:36.6	-1:40:08	24623 \pm 43	2
13:30:50.8	-1:51:37	26088 \pm 26	1,2	13:31:37.7	-1:52:25	26268 \pm 39	1
13:30:53.0	-1:37:31	24965 \pm 30	1	13:31:49.5	-1:58:52	26610 \pm 31	1
13:30:54.2	-1:52:33	26512 \pm 31	1,2	13:31:50.1	-1:57:38	27081 \pm 30	1
13:30:55.6	-1:55:13	23632 \pm 43	1	13:31:50.9	-1:41:15	24889 \pm 35	1
13:30:56.3	-1:54:08	26873 \pm 50	2	13:31:52.1	-1:56:07	26789 \pm 28	1
13:30:56.4	-1:42:20	27244 \pm 50	2	13:31:54.4	-1:43:44	25915 \pm 21	1
13:30:56.6	-1:43:24	24704 \pm 23	1,2	13:31:56.7	-1:49:35	22697 \pm 44	1
13:30:56.7	-1:53:58	25515 \pm 29	1,2	13:32:15.5	-1:43:13	26803 \pm 22	1

REFERENCES.— (1) LCO-SHECTOGRAPH; (2)Beers et al. 1991

TABLE 5
ABELL 3395 VELOCITIES

α (J2000)	δ (J2000)	v (km s $^{-1}$)	Reference	α (J2000)	δ (J2000)	v (km s $^{-1}$)	Reference
6:24:23.2	-54:29:48	14478 \pm 105	1	6:27:23.7	-54:28:23	15743 \pm 70	1,2
6:24:26.9	-54:32:55	15741 \pm 71	1	6:27:24.4	-54:26:30	14440 \pm 32	2
6:24:30.1	-54:07:36	15338 \pm 69	1	6:27:26.6	-54:25:48	15099 \pm 30	1,2
6:24:32.2	-54:10:04	14012 \pm 49	1	6:27:26.3	-54:31:02	15735 \pm 42	1,4,7
6:24:35.6	-54:07:47	14324 \pm 48	1	6:27:29.8	-54:27:19	15024 \pm 52	1,4
6:24:38.8	-54:14:18	14410 \pm 101	1	6:27:30.5	-54:35:48	17949 \pm 39	1,2
6:24:48.9	-54:14:48	13808 \pm 242	1,2,3	6:27:36.1	-54:24:05	14675 \pm 72	1
6:24:60.0	-54:10:31	17463 \pm 30	1,2	6:27:36.3	-54:26:58	14562 \pm 30	1,2,5,7
6:25:04.0	-54:22:21	13835 \pm 91	1,2	6:27:35.6	-54:40:04	16106 \pm 77	1
6:25:04.8	-54:09:41	17625 \pm 110	1	6:27:38.2	-54:25:50	16486 \pm 118	1
6:25:09.3	-54:25:01	17570 \pm 44	1,2	6:27:39.1	-54:22:38	13754 \pm 925	1,4
6:25:15.3	-54:16:15	17670 \pm 276	1,2	6:27:39.4	-54:27:43	14676 \pm 30	1,2
6:25:20.1	-54:21:36	14502 \pm 108	1	6:27:40.0	-54:26:55	16222 \pm 34	2
6:25:22.4	-54:16:54	17504 \pm 57	1,4	6:27:41.0	-54:27:15	17046 \pm 71	1,4,5
6:25:31.5	-54:34:41	15088 \pm 105	1	6:27:41.3	-54:23:48	16553 \pm 131	1
6:25:48.3	-54:11:43	14293 \pm 82	1,4	6:27:40.5	-54:36:50	15676 \pm 47	1
6:25:49.1	-53:59:36	13910 \pm 89	1,5	6:27:41.9	-54:17:25	14342 \pm 78	1
6:25:47.8	-54:39:53	16401 \pm 76	1	6:27:40.9	-54:35:34	15465 \pm 170	1,3
6:25:51.2	-54:18:22	16134 \pm 88	1	6:27:42.0	-54:32:19	15245 \pm 163	1,2
6:25:57.0	-54:27:50	18047 \pm 91	1,3,4	6:27:44.3	-54:07:10	14912 \pm 163	1,2
6:25:58.4	-54:27:44	18263 \pm 35	2	6:27:44.2	-54:16:51	16158 \pm 83	1
6:26:01.0	-54:27:40	18153 \pm 139	1	6:27:43.8	-54:24:26	13712 \pm 33	1,2
6:26:08.7	-54:22:04	14777 \pm 92	1	6:27:43.7	-54:27:19	16248 \pm 73	1,4,5
6:26:07.9	-54:40:30	15499 \pm 79	1,2,6	6:27:44.6	-54:26:45	13265 \pm 84	1,2,5
6:26:10.3	-54:27:24	15670 \pm 43	1,2	6:27:47.0	-54:25:10	16305 \pm 201	1,3,4
6:26:10.4	-54:32:26	16418 \pm 56	1,2	6:27:47.6	-54:25:28	14872 \pm 52	1
6:26:11.5	-54:17:14	14960 \pm 33	4	6:27:49.1	-54:04:03	17986 \pm 41	2
6:26:12.0	-54:17:08	15224 \pm 42	2	6:27:48.6	-54:32:19	13076 \pm 55	4
6:26:12.1	-54:23:40	14230 \pm 106	1	6:27:50.9	-54:09:05	14586 \pm 69	1
6:26:11.4	-54:40:16	17627 \pm 98	1	6:27:51.1	-54:09:07	14926 \pm 223	1,2
6:26:13.7	-54:24:19	17728 \pm 30	1,2	6:27:50.7	-54:28:22	15535 \pm 55	1,2
6:26:15.2	-54:19:37	14659 \pm 75	1	6:27:52.5	-54:30:04	14322 \pm 311	1,4
6:26:16.8	-54:20:17	14911 \pm 31	1,2	6:27:52.1	-54:36:52	16616 \pm 104	1
6:26:17.3	-54:32:26	15887 \pm 81	1,2	6:27:54.5	-54:31:24	16152 \pm 166	1,2
6:26:20.7	-54:15:32	14543 \pm 112	1,2,3	6:27:56.3	-54:26:02	13983 \pm 66	4
6:26:24.1	-54:20:38	14755 \pm 77	1,2	6:27:58.5	-54:32:50	16143 \pm 188	1
6:26:27.4	-54:28:35	14797 \pm 98	1	6:27:59.3	-54:29:44	15097 \pm 104	1,2
6:26:30.5	-54:17:57	13248 \pm 81	1	6:28:01.4	-54:35:09	15360 \pm 94	1
6:26:31.5	-54:36:55	14172 \pm 50	2	6:28:02.0	-54:34:14	14153 \pm 89	1,2
6:26:32.4	-54:34:01	16305 \pm 30	2	6:28:05.8	-54:24:12	15033 \pm 35	1
6:26:34.3	-54:10:00	13544 \pm 78	1,2	6:28:08.0	-54:34:18	15530 \pm 76	1,2
6:26:34.7	-54:09:50	14621 \pm 35	2	6:28:13.2	-54:15:35	16437 \pm 39	1,2
6:26:34.5	-54:21:25	15264 \pm 202	1,3,4	6:28:12.5	-54:29:47	16163 \pm 48	2
6:26:34.6	-54:25:56	15548 \pm 69	1	6:28:15.2	-54:35:23	15793 \pm 134	1,2,7
6:26:35.8	-54:29:31	15853 \pm 51	1,3,4	6:28:16.6	-54:31:39	15909 \pm 74	1,2,7
6:26:37.5	-54:26:02	14542 \pm 150	1,4	6:28:18.7	-54:15:09	15686 \pm 99	1,3,4
6:26:40.1	-54:12:03	15623 \pm 81	1	6:28:18.9	-54:21:36	14548 \pm 72	1
6:26:40.2	-54:11:23	17655 \pm 115	1	6:28:20.3	-54:36:38	14983 \pm 153	1,2
6:26:40.0	-54:20:02	14139 \pm 30	1,2	6:28:21.2	-54:25:25	15451 \pm 238	1,2
6:26:40.4	-54:32:48	18213 \pm 49	2	6:28:23.1	-54:20:00	14591 \pm 102	1
6:26:43.4	-54:19:14	14675 \pm 896	1,2	6:28:23.2	-54:35:55	15432 \pm 47	1,2
6:26:43.5	-54:26:16	15500 \pm 116	1	6:28:29.1	-54:22:48	14685 \pm 272	1,2,3
6:26:47.9	-54:24:06	13626 \pm 30	1,2,3	6:28:30.0	-54:16:23	15412 \pm 62	1,4
6:26:49.5	-54:32:34	15622 \pm 58	1,2,3	6:28:34.6	-54:28:05	15564 \pm 142	1,2
6:26:51.0	-54:32:48	15003 \pm 40	1,2	6:28:46.8	-54:23:25	14313 \pm 63	1

The authors would like to thank Dan Fabricant for helpful comments. RHD, WF, CJ acknowledge support from the Smithsonian Institute and NASA contract NAS8-

39073. HQ acknowledges partial support from FONDECYT grant 8970009 and the award of a Presidential Chair in Science (Chile).

REFERENCES

Abell, G.O., Corwin, H.G. & Olowin, R.P. 1989, *ApJS*, 70, 1.

Arnaud, K. 1993, *ASCA* Newsletter, No. 1 (NASA/GSFC).

Arnaud, M., Neumann, D.M., Aghanim, N., Gastaud, R., Majerowicz, S., & Hughes, J.P. 2001, *A&A*, 365, L80.

Beers, T.C., Geller, M.J. & Huchra, J.P. 1982, *ApJ*, 257, 23.

Beers, T.C., Flynn, K., & Gebhardt, K. 1990, *AJ*, 100, 32.

Beers, T., Forman, W., Huchra, J., Jones, C. & Gebhardt, K. 1991, *AJ*, 102, 1581.

Bird, C. M. 1994, *AJ*, 107, 1637.

Cavaliere, A. & Fusco-Femiano, R. 1976, *A&A*, 49, 137.

Churazov, E., Gilfanov, M., Forman, W. & Jones, C. 1996, *ApJ*, 471, 673.

Churazov, E., Gilfanov, M., Forman, W. & Jones, C. 1999, *ApJ*, 520, 105.

David, L.P., Arnaud, K.A., Forman, W. & Jones, C. 1990, *ApJ*, 356, 32.

Donnelly, R., Hank, Markevitch, M., Forman, W., Jones, C., Churazov, E. & Gilfanov, M. 1999, *ApJ*, 513, 690.

Donnelly, R., Hank, Markevitch, M., Forman, W., Jones, C., David, L.P., Churazov, E. & Gilfanov, M. 1998, *ApJ*, 500, 138.

Dressler, A. & Shectman, S. A. 1988, *AJ*, 985.

Einasto, M., Tago, E., Jaaniste, J., Einasto, J., & Andernach, H. 1997, *A&AS*, 123, 119.

Evrard, A. E. 1990a, *ApJ*, 363, 349.

Evrard, A. E. 1990b, in *Clusters of Galaxies*, eds. Oegerle, Fitchett and Danly (Cambridge: Cambridge University Press), 287.

Evrard, A.E., Metzler, C.A. & Navarro, J.F. 1996, *ApJ*, 469, 490.

Fabricant, D.G., Bautz, M.W. & McClintock, J.E. 1994, *AJ*, 107, 8.

Forman, C. & Jones, C. 1990, in *Clusters of Galaxies*, ed. W. Oegerle, M. Fitchett, & L. Danly (Cambridge: Cambridge Univ. Press), 257.

Forman, W., Bechtold, J., Blair, W., Giacconi, R., Van Speybroeck, L., & Jones, C. 1981, *ApJL*, 243, L133.

Geller, M.J., & Beers, T.C. 1982, *PASP*, 94, 421.

Henriksen, M., Donnelly, R., Hank & Davis, D. 2000, *ApJ*, 529, 692.

Henriksen, M. & Markevitch, M. 1996, *ApJL*, 466, L79.

Henry, J.P. & Briel, U.G. 1995, *ApJL*, 443, L9.

Hopp, U. and Materne, J. 1985, *A&A*, 148, 359.

Jones, C. & Forman, W.R. 1999, *ApJ*, 511, 65.

Jones, C. & Forman, W.R. 1984, *ApJ*, 276, 38.

Katgert, P., Mazure, A., Perea, J., den Hartog, R., Moles, M., Le Fevre, O., Dubath, P., Focardi, P., Rhee, G., Jones, B., Escalera, E., Biviano, A., Gerbal, D. & Giuricin, G. 1996, *A&A*, 310, 8.

Katgert, P., Mazure, A., den Hartog, R., Adami, C., Biviano, A., and Perea, J. 1998, *A&AS*, 129, 399.

Maddox, S.J., Efstathiou, G., Sutherland, W.J. and Loveday, J. 1990, *MNRAS*, 243, 692.

Markevitch, M., Ponman, T. J., Nulsen, P.E.J., Bautz, M.W., Burke, D.J., David, L.P., Davis, D., Donnelly, R.H., Forman, W.R., Jones, C., Kaastra, J., Kellogg, E., Kim, D.-W., Kolodziejczak, J., Mazzotta, P., Pagliaro, A., Patel, S., Van Speybroeck, L., Vikhlinin, A., Vrtilek, J., Wise, M. & Zhao, P. 2000, *ApJ*, 541, 542.

Markevitch, M., Vikhlinin, A., Forman, W.R & Sarazin, C.L. 1999, *ApJ*, 527, 545.

Markevitch, M., Forman, W.R., Sarazin, C.L. & Vikhlinin, A. 1998, *ApJ* 503, 77.

Markevitch, M., Sarazin, C. & Irwin, J.A. 1996a, *ApJ*, 472, L17.

Markevitch, M., Mushotzky, R., Inoue, H., Yamashita, K., Furuzawa, A., & Tawara, Y. 1996b, *ApJ*, 456, 437.

Materne, J., Chincarini, G., Tarenghi, M. & Hopp, U. 1982, *A&A*, 109, 238.

Mohr, J., Fabricant, D.G., Geller, M. J., and Evrard, A.E. 1995, *ApJ*, 447, 8.

Mohr, J.J., Reese, E.D., Ellingson, E., Lewis, A.D. & Evrard, A.E. 2000, *ApJ*, 544, 109.

Norman, M.L. & Bryan, G.L. 1999, in "The Radio Galaxy Messier 87", ed. Röser, H.-J. & Meisenheimer, K. (New York, Springer), p. 106.

Quintana H., Ramírez A., 1990, *AJ*, 100, 1424.

Quintana H., Ramírez, A., Melnick, J., Raychaudhury, S., & Slezak, E. 1995, *AJ*, 110, 463.

Quintana H., Ramírez, A., & Way M.J. 1996, *AJ*, 112, 36. .

Quintana H., Carrasco, E.R., & Reisenegger, A. 2000, *AJ*, 120, 511.

Raychaudhury, S., Fabian, A.C., Edge, A.C., Jones, C. & Forman, W. 1991, *MNRAS*, 248, 101.

Richstone, Loeb & Turner 1992, *ApJ*, 393, 477.

Ricker, P.M. 1998, *ApJ*, 496, 670.

Roettiger, K., Burns, J.O., & Loken, C. 1996, *ApJ*, 473, 651.

Roettiger, K., Loken, C. & Burns, J.O. 1997, *ApJS*, 109, 307.

Schindler, S., & Müller, E. 1993, *A&A*, 272, 137.

Slezak, E., Durret, F. & Gerbal, D. 1994, *AJ*, 108, 1996.

Snowden, S.L. 1994, *Cookbook for Analysis Procedures for ROSAT XRT/PSPC Observations of Extended Objects and the Diffuse Background*.

Snowden, S.L., McCammon, D., Burrows, D.N. & Mendenhall, J.A. 1994, *ApJ*, 424, 714.

Struble, M.F. & Rood, H.J. 1999, *ApJS*, 125, 35.

Takahashi, T., Markevitch, M., Fukuzawa, Y., Ikebe, Y., Ishiaki, Y., Kikuchi, K., Makishimi, K. & Tarawa, Y. 1995, *ASCA* Newsletter, No. 3 (NASA/GSFC).

Teague, P.F., Carter, D. & Gray, P. 1990, *ApJS*, 72, 715

Vidal, N.V. 1975 *PASP*, 87, 625

Vikhlinin, A., Forman, W. & Jones, C. 1999, *ApJ*, 525, 47.

West and Frandsen 1981, *A&AS*, 44, 329

White, D.A., Jones, C. & Forman, W. 1997, *MNRAS*, 292, 419.

White, D.A. 1999 *private communication*.

TABLE 5—Continued

α (J2000)	δ (J2000)	v (km s $^{-1}$)	Reference	α (J2000)	δ (J2000)	v (km s $^{-1}$)	Reference
6:26:52.0	-54:28:52	15503 \pm 64	1,2	6:28:49.1	-54:28:16	13447 \pm 40	1
6:26:53.6	-54:35:07	15445 \pm 95	1	6:28:57.2	-54:17:17	15847 \pm 30	1,2
6:26:54.9	-54:19:14	14076 \pm 101	1	6:29:00.2	-54:12:41	14836 \pm 163	1,2
6:26:57.8	-54:33:31	15877 \pm 31	1,2	6:28:59.7	-54:22:12	15088 \pm 158	1,2
6:26:58.7	-54:28:09	15432 \pm 92	1	6:28:59.8	-54:23:03	14561 \pm 31	2
6:27:04.7	-54:25:47	15095 \pm 146	1	6:29:03.0	-54:23:12	14977 \pm 94	1,2,5,7
6:27:06.5	-54:22:15	15026 \pm 180	1,2	6:29:09.9	-54:26:00	15003 \pm 186	1,2
6:27:06.1	-54:33:26	15036 \pm 159	1,2	6:29:27.0	-54:27:03	14678 \pm 39	2
6:27:07.0	-54:26:40	16212 \pm 113	1	6:29:33.4	-54:15:26	13311 \pm 94	1,4
6:27:08.8	-54:05:31	15300 \pm 34	1,2,3,4	6:29:37.2	-54:42:46	13856 \pm 71	4
6:27:08.8	-54:22:25	16412 \pm 39	1,2,3	6:29:44.7	-54:36:25	14510 \pm 48	1,2
6:27:09.0	-54:26:45	14930 \pm 77	1	6:29:47.1	-54:48:18	14912 \pm 69	1,2,3
6:27:10.4	-54:20:08	15537 \pm 113	1	6:29:47.6	-54:47:48	15110 \pm 73	2,3
6:27:15.0	-54:00:03	15362 \pm 88	1	6:30:06.6	-54:35:13	14506 \pm 50	1
6:27:14.6	-54:08:34	16238 \pm 69	1,4	6:30:09.9	-54:17:22	15243 \pm 49	1
6:27:14.8	-54:25:34	14849 \pm 72	1,2	6:30:15.6	-54:20:56	16162 \pm 150	1
6:27:16.1	-54:23:00	16624 \pm 32	1,2	6:30:24.3	-54:41:02	14686 \pm 81	1
6:27:16.4	-54:32:07	15808 \pm 31	1,2	6:30:25.4	-54:26:47	13911 \pm 181	1
6:27:19.4	-54:06:58	17444 \pm 36	1,4	6:30:25.6	-54:45:45	14970 \pm 43	1,2
6:27:18.9	-54:24:06	15609 \pm 123	4	6:30:29.3	-54:33:22	15377 \pm 123	1
6:27:19.2	-54:25:15	13657 \pm 40	1,4	6:30:28.9	-54:41:06	14959 \pm 67	1
6:27:19.7	-54:28:31	14766 \pm 262	1,4	6:30:36.3	-54:44:07	14312 \pm 106	1
6:27:19.6	-54:37:00	14560 \pm 80	4	6:30:51.2	-54:26:00	13432 \pm 85	1
6:27:21.0	-54:26:20	16430 \pm 30	1,2,4				

REFERENCES.— (1) Teague et al. 1990 with 82 km s $^{-1}$ offset; (2) LCO-SHECTOGRAPH; (3) Hopp and Materne 1985; (4) CTIO-ARGUS with 50 km s $^{-1}$ offset; (5) Materne et al. 1982; (6) West and Frandsen 1981; (7) Vidal 1975

TABLE 6
COMPOSITE VELOCITY RESULTS

Cluster	\bar{v} (km s $^{-1}$)	σ (km s $^{-1}$)	V_r (km s $^{-1}$)
Abell 3528	16346 \pm 118	985 \pm 101	
SE	16040 \pm 318	930 \pm 255(516 \pm 151) ^a	
NW	16136 \pm 207	969 \pm 198	96 $^{+379}_{-96}$
Abell 1750	25632 \pm 132	1050 \pm 96	
NE	24815 \pm 153	676 \pm 310	
SW	26150 \pm 145	906 \pm 236	1335 \pm 211
Abell 3395	15177 \pm 118	1069 \pm 81	
NE all	15325 \pm 167	949 \pm 103	
SW all	15427 \pm 135	713 \pm 185	102 $^{+214}_{-102}$
NE clip	15244 \pm 165	1036 \pm 107	
SW clip	15436 \pm 169	939 \pm 311	192 $^{+236}_{-192}$

^aThe parenthetical value excludes the two galaxies with highly discrepant velocities.

TABLE 7
MASS^aDETERMINATIONS

Cluster	M_{gas}		M_{total}		$M_{isothermal}$	M_{scaled}	M_{virial}
	0.5 Mpc	1.0 Mpc	0.5 Mpc	1.0 Mpc	1.0 Mpc	1.0 Mpc	Total
A3528 SE	$0.37^{+0.01}_{-0.01}$	$1.06^{+0.02}_{-0.02}$	1.7^{+2}_{-1}	3.6^{+3}_{-3}	2.8^{+1}_{-2}	4.4^{+3}_{-3}	$6.6^{+4.1}_{-3.1}(2.27^{+1.5})^b$
A3528 NW	$0.31^{+0.01}_{-0.01}$	$0.86^{+0.02}_{-0.01}$	1.9^{+2}_{-2}	4.0^{+3}_{-4}	3.0^{+1}_{-2}	4.3^{+4}_{-4}	$4.5^{+2.1}_{-1.6}$
A1750 NE	$0.28^{+0.01}_{-0.01}$	$0.90^{+0.02}_{-0.02}$	1.3^{+1}_{-1}	2.7^{+3}_{-3}	2.2^{+1}_{-2}	3.7^{+4}_{-4}	$2.0^{+2.3}_{-1.4}$
A1750 SW	$0.36^{+0.01}_{-0.01}$	$1.03^{+0.02}_{-0.02}$	1.5^{+2}_{-1}	3.4^{+3}_{-4}	2.7^{+1}_{-2}	3.6^{+4}_{-3}	$4.0^{+2.3}_{-1.1}$
A3395 NE	$0.30^{+0.01}_{-0.01}$	$1.00^{+0.02}_{-0.02}$	1.6^{+1}_{-2}	3.8^{+3}_{-3}	3.0^{+1}_{-1}	4.2^{+4}_{-3}	$4.5^{+1.1}_{-0.9}$
A3395 SW	$0.30^{+0.01}_{-0.01}$	$1.04^{+0.02}_{-0.02}$	1.5^{+1}_{-2}	3.4^{+3}_{-3}	2.6^{+1}_{-2}	4.2^{+5}_{-3}	$3.1^{+1.8}_{-1.4}$

^aMasses are all in units of $10^{14} M_{\odot}$.

^bThe parenthetical value excludes the two galaxies with highly discrepant velocities.

FIG. 1.— *Top left*: Continuous temperature map for A3528 from *ASCA* GIS data with intensity contours and region identifiers overlaid. *Bottom left*: Fit temperatures with 90% confidence error bars for the regions defined on the continuous temperature map. The global cluster temperature is show as a dotted line. *Top right*: Galaxies with redshifts are overlain on the *ROSAT* intensity contours. Galaxies with velocities greater than the overall mean cluster velocity are shown in red and those with smaller velocities are in blue. The field-of-view for the top right has been expanded to include all of the galaxies listed in Table 4 and shown in the lower right. The outline of the top left frame is shown as a dashed line. Circles denoting a radius of a half Mpc are shown centered on each sub-cluster core and are color coded to match the sub-cluster histograms shown in the bottom right. *Bottom right*: Velocity histogram of the galaxies shown in the top right. Bins are 300 km s⁻¹ wide and the overall cluster velocity is indicated by a dashed line.

FIG. 2.— Same as for Figure 1 for Abell 1750. The field-of-view for the top right has been expanded to include all of the galaxies listed in Table 4 and shown in the lower right; the outline of the top left frame is shown as a dashed line. The half Mpc circles in the top right are color coded to match the velocity histograms of the sub-cluster cores shown in the bottom right.

FIG. 3.— Same as for Figure 1 for Abell 3395. The field-of-view for the top right has been expanded to include all of the galaxies listed in Table 5 and shown in the lower right; the outline of the top left frame is shown as a dashed line. The half Mpc circles in the top right are color coded to match the velocity histograms of the sub-cluster cores shown in the bottom right. The galaxies in the high velocity bump in the bottom right are shown as empty circles in the top right panel.

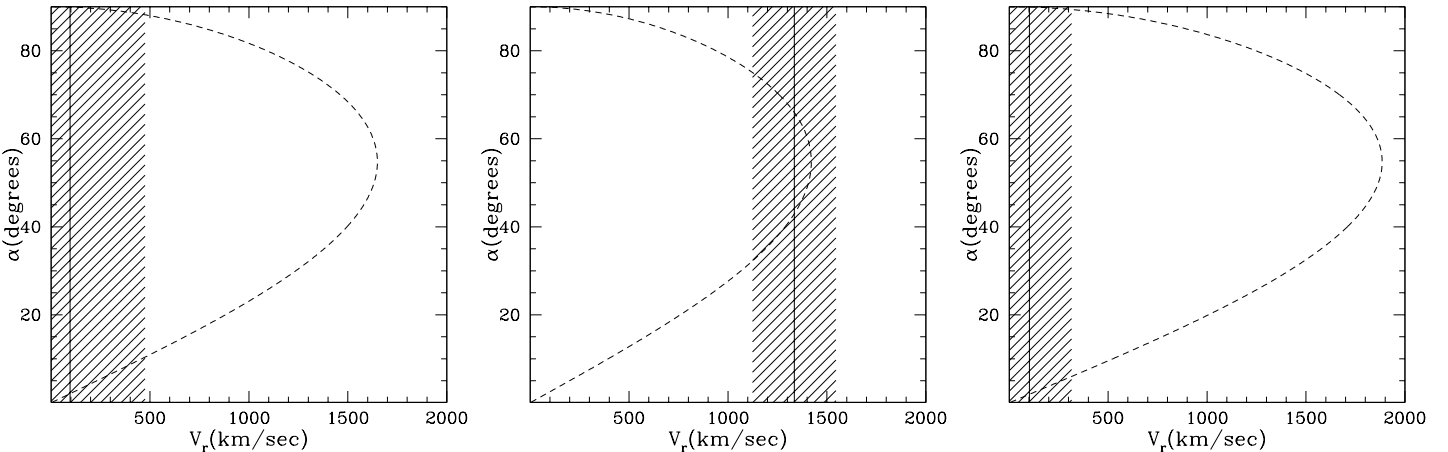


FIG. 4.— Plots of simple Newtonian energy binding conditions as a function of measured relative velocity (V_r) and projection angle from the plane of the sky (α) for Abell 3528 (left), 1750 (middle) and 3395 (right). The dashed lines are the limiting cases for bound systems, thus all orbit solutions to the right are unbound, while those to the left are bound. The measured relative velocity from our data is indicated by the solid vertical lines and its 68% confidence region is shown with the cross-hatching.

This figure "a1750.gif" is available in "gif" format from:

<http://arxiv.org/ps/astro-ph/0106482v1>

This figure "a3395.gif" is available in "gif" format from:

<http://arxiv.org/ps/astro-ph/0106482v1>

This figure "a3528.gif" is available in "gif" format from:

<http://arxiv.org/ps/astro-ph/0106482v1>